JOURNAL OF APPLIED CRYSTALLOGRAPHY
ISSN 1600-5767

X-ray ptychographic mode of self-assembled CdSe/CdS octapod-shaped nanocrystals in thick polymers[1]

Liberato De Caro,[a] Francesco Scattarella,[a] Davide Altamura,[a] Milena P. Arciniegas,[b] Dritan Siliqi,[a] Liberato Manna[b] and Cinzia Giannini[a]*

[a]Istituto di Cristallografia, CNR, via Amendola 122/O, Bari, Italy, and [b]Nanochemistry Department, Istituto Italiano di Tecnologia, via Morego 30, Genova, Italy. *Correspondence e-mail: cinzia.giannini@ic.cnr.it

Received 11 January 2020
Accepted 27 April 2020

Edited by D. Shapiro, Lawrence Berkeley National Laboratory, USA

[1] This article will form part of a virtual special issue of the journal on ptychography software and technical developments.

Keywords: nanomaterials; polymers; X-ray ptychography; X-ray microscopy; X-ray imaging.

This work describes the application of X-ray ptychography for the inspection of complex assemblies of highly anisotropic nanocrystals embedded in a thick polymer matrix. More specifically, this case deals with CdSe/CdS octapods, with pod length $L = 39 \pm 2$ nm and pod diameter $D = 12 \pm 2$ nm, dispersed in free-standing thick films (24 ± 4 µm) of polymethyl methacrylate and polystyrene, with different molecular weights. Ptychography is the only imaging method available to date that can be used to study architectures made by these types of nanocrystals in thick polymeric films, as any other alternative direct method, such as scanning/transmission electron microscopy, can be definitively ruled out as a result of the large thickness of the free-standing films. The electron density maps of the investigated samples are reconstructed by combining iterative difference map algorithms and a maximum likelihood optimization algorithm. In addition, post image processing techniques are applied to both reduce noise and provide a better visualization of the material morphological details. Through this process, at a final resolution of 27 nm, the reconstructed maps allow us to visualize the intricate network of octapods inside the polymeric matrices.

1. Introduction

Colloidal nanoparticles (NPs) and nanocrystals (NCs) are typically composed of an inorganic core surrounded by an organic shell of surfactants. They are typically processed by wet chemistry (Alivisatos, 1997), which adopts simple fabrication routes to produce nanomaterials even on a large scale. Their size may be varied between 1 and 100 nm, which means they can be synthesized in a range bridging clusters of atoms to bulk-like materials. Thermodynamics rules the formation of NCs with a variety of shapes, as illustrated in Fig. 1(*a*), from solid and hollow spheres, rods, flat discs, dumbbells and cubes, to tetrapods or even more complex morphologies. Their properties strongly depend on their size and shape (Peng *et al.*, 2000; Scher *et al.*, 2003). In terms of applications, colloidal semiconducting chalcogenides (Rogach *et al.*, 2008) and perovskite quantum dots (Akkerman *et al.*, 2018) have been widely investigated for solar cells (Noel *et al.*, 2014; Akkerman *et al.*, 2016), metal NCs (Au, Ag, Co) in nanoplasmonics (Genç *et al.*, 2017; Tao *et al.*, 2008), and metal or magnetic NCs for biosensing and cellular imaging (Parak *et al.*, 2003). The high surface-to-bulk ratio makes them also suitable for catalytic applications: see for example the TiO_2 case (Gupta & Tripathi, 2011; Dahl *et al.*, 2014; Petronella *et al.*, 2017). The surfactants that are passivating the NC surfaces, apart from limiting the crystal growth, also mediate the surface interactions and offer a means to tune the NC functionality.

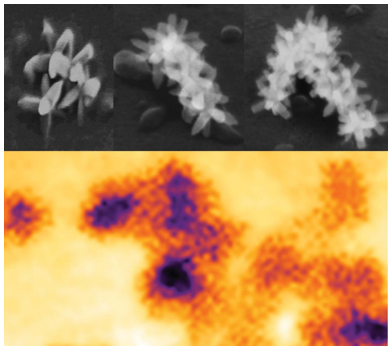

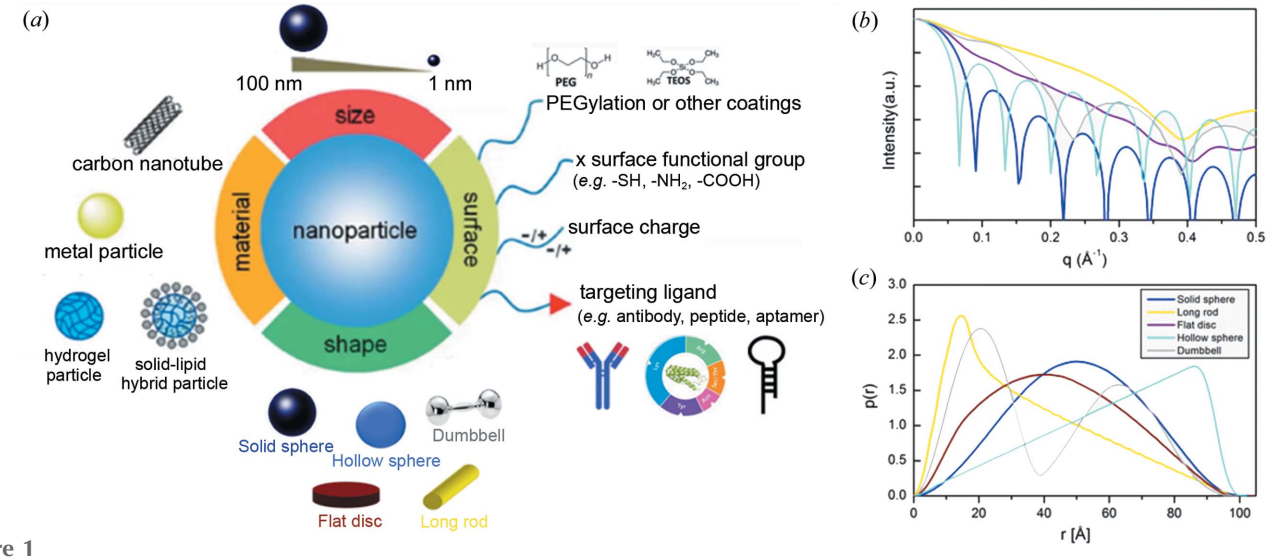

Figure 1
(*a*) Schematic description of a nanoparticle defined by a specific material (*e.g.* carbon nanotube, metal particle, hydrogel particle, solid–lipid hybrid particle), a characteristic size (here from 1 to 100 nm) and shape (solid and hollow sphere, rod, disc, dumbbell), a surface charge (negative or positive), and a surface functional group (here PEG, antibodies, peptides *etc.*); (*b*) SAXS profiles computed for the different shapes in (*a*), following the same color code; (*c*) pair distribution functions computed for the shapes in (*a*) and corresponding to the SAXS profiles in (*b*).

To characterize NPs and NCs, X-ray-based techniques such as X-ray diffraction (XRD) (Kumar, 2016: Giannini *et al.*, 2016; Mino *et al.*, 2018; Giannini *et al.*, 2020), small/wide-angle X-ray scattering (SAXS/WAXS) (Gordon *et al.*, 2015; Craievich, 2016; Glatter, 2018) – including the grazing incidence (GI) versions GISAXS/GIWAXS (Muller-Buschbaum, 2003; Renaud *et al.*, 2009; Altamura, Sibillano *et al.*, 2012) – and the pair distribution function (PDF) (Juhás *et al.*, 2006; Billinge & Levin, 2007) are typically used. These techniques are needed to answer basic questions such as what is (are) the crystal structure(s) of the particles; what is the particle/domain size (and size distribution); and what is the particle/domain shape? The choice of the appropriate technique depends, in part, on the state of the materials, as they can be produced in powders (suitable for XRD and PDF), embedded in films and free-standing membranes (convenient for SAXS/WAXS), anchored on top of surfaces (ideal for GISAXS/GIWAXS), or dispersed in liquids (to analyze via SAXS/WAXS). When PDF analysis becomes mandatory, data must generally be collected at dedicated beamlines [*e.g.* the P02.1 beamline at PETRA III or the 28-ID-1 beamline of the National Synchrotron Light Source (NSLS-II) at Brookhaven National Laboratory], although high-brilliance laboratory equipment has recently appeared on the market (Reiss *et al.*, 2012; Sommariva, 2013). For the microstructural analysis of the material (domain size and shape), considering that single NPs can consist of multiple crystalline domains, SAXS/GISAXS allow us to identify the average particle size/shape whereas WAXS/GIWAXS/XRD permit us to measure the average domain extension (size/shape) of the nanocrystalline component only. For example, for the colloidal NP of interest displayed in Fig. 1(*a*), which is depicted here schematically as a core inorganic structure (carbon nanotube, metal particle, hydrogel particle, solid–lipid hybrid particle), with a characteristic size (here from 1 to 100 nm) and shape (solid and hollow sphere, rod, disc, dumbbell), surface charge (negative or positive), and surface functional group (here PEG, antibodies, peptides *etc.*), the calculated SAXS profiles [Fig. 1(*b*)] and relative pair distribution functions [Fig. 1(*c*)] change with the corresponding NP shape [Fig. 1(*a*), same color code (Svergun & Koch, 2003)]. This comparison shows how SAXS can be efficient in assessing the average particle shape, clearly distinguishing among all of the possible shapes independently of the particle crystallinity. We note that it is also possible to discern between hollow and solid spheres via SAXS analysis, which is relevant for instance when hollow nanospheres are used as drug carriers (Blanco *et al.*, 2001).

Once control over the shape and size of NPs and NCs was achieved to produce monodispersed particles of specific shapes, researchers started to assemble them in periodically ordered nanostructures. These efforts led to a variety of superlattices with a specific NP or NC as the repeat unit in one-, two- or three-dimensional structures. In most cases, they were self-assembled (Damasceno *et al.*, 2012; Boles *et al.*, 2016) on the basis of their shape (Paik & Murray, 2013; Castelli *et al.*, 2016) or by using an external field [*e.g.* a magnetic field in the work by Altamura, Holý *et al.* (2012)]. In these cases, GISAXS and GIWAXS were adopted to study, often within the same experiment, the structure, size and crystalline domain shape of the building blocks (GIWAXS), as well as of the entire assembled superlattice (GISAXS). Also, *in situ* experiments were conducted with the aim of following the kinetics of the assembly process (Corricelli *et al.*, 2014; Yu *et al.*, 2018). In addition, monodispersed NPs or NCs of specific shapes were merged together in aperiodic architectures, forming end-to-end assemblies (Talapin *et al.*, 2009; Boles *et al.*, 2016). Non-periodic networks are invisible to all the previously cited X-ray techniques, if the relevant information to extract

concerns the assembly itself and not the single building blocks (although GISAXS can still be used to study the overall morphology of the NPs and NCs). In these particuliar cases, hard X-ray lens-less techniques to image extended objects are extremely useful (Rodenburg *et al.*, 2007; Nugent, 2010; Shi *et al.*, 2019). The use of electron microscopy or scanning transmission microscopy with soft X-rays (Shapiro *et al.*, 2014) is not feasible here due to the thick 24 µm polymer matrix in which the NPs are embedded. Therefore, hard X-ray microscopy with phase contrast appears to be the only solution to visualize the arrangements of these NPs. X-ray ptychography in two dimensions has been successfully used to reveal the arrangement of NCs made of a CdSe core with eight CdS pods, so called octapods, and assembled in an irregular architecture to create a non-periodic network embedded in polystyrene (PS) free-standing polymer film with a thickness of 24 µm (De Caro *et al.*, 2016). In the present work, using the same phase retrieval scheme and post-pashing data treatment approaches (*i.e.* deblurring and denoising methods to improve the retrieved phase images), we include further results of similar NCs embedded in a polymethyl methacrylate (PMMA) matrix. The very large thickness of the polymeric matrix excludes any direct imaging technique such as transmission/scanning electron microscopy (TEM/SEM) to inspect the real status of the octapod assembly. The expected aperiodic network of the octapods also rules out any traditional scattering technique (SAXS/GISAXS). Indeed, GISAXS data were collected and the diffraction patterns were interpreted as the scattering of the octapod shape only, or were useful only in the case of periodic assembly of octapods without any polymeric matrix (De Caro *et al.*, 2016).

2. Sample description

Octapod-shaped NCs were synthesized following a standard procedure (Kim *et al.*, 2012) and dispersed in toluene. The solution was washed four times to remove the excess surfactants by adding MeOH (1:0.5; toluene:MeOH volume ratio) followed by heating at 343 K for 5 min and centrifugation at 3000 r min^{-1} for 3 min. The final precipitate was dispersed in toluene and sonicated for 10 min. Fig. 2(*a*) shows a 3D reconstruction from STEM analysis of the CdSe/CdS octapods studied here, which have a pod length $L = 39 \pm 2$ nm and a pod diameter $D = 12 \pm 2$ nm. A typical periodically assembled region of octapods, shown in Fig. 2(*b*), was investigated in previous work (De Caro *et al.*, 2012). Conversely, interlocked octapods, self-assembled in aperiodic linear architectures, can be also formed, as imaged by SEM and shown in Figs. 2(*c*)–2(*h*).

To prepare the octapod–polymer free-standing films, the polymers were first dissolved in toluene with a concentration of 5% in volume. Table 1 presents the two polymers used here; the polymers were purchased from Sigma–Aldrich.

The polymer solutions were kept under strong shaking for 5 h and then filtered through a 0.45 µm polytetrafluoroethylene filter prior to use. The nanocomposite solutions were prepared by adding 300 µl of the octapod solution to 200 µl of polymer solution at 5% for a final polymer concentration of

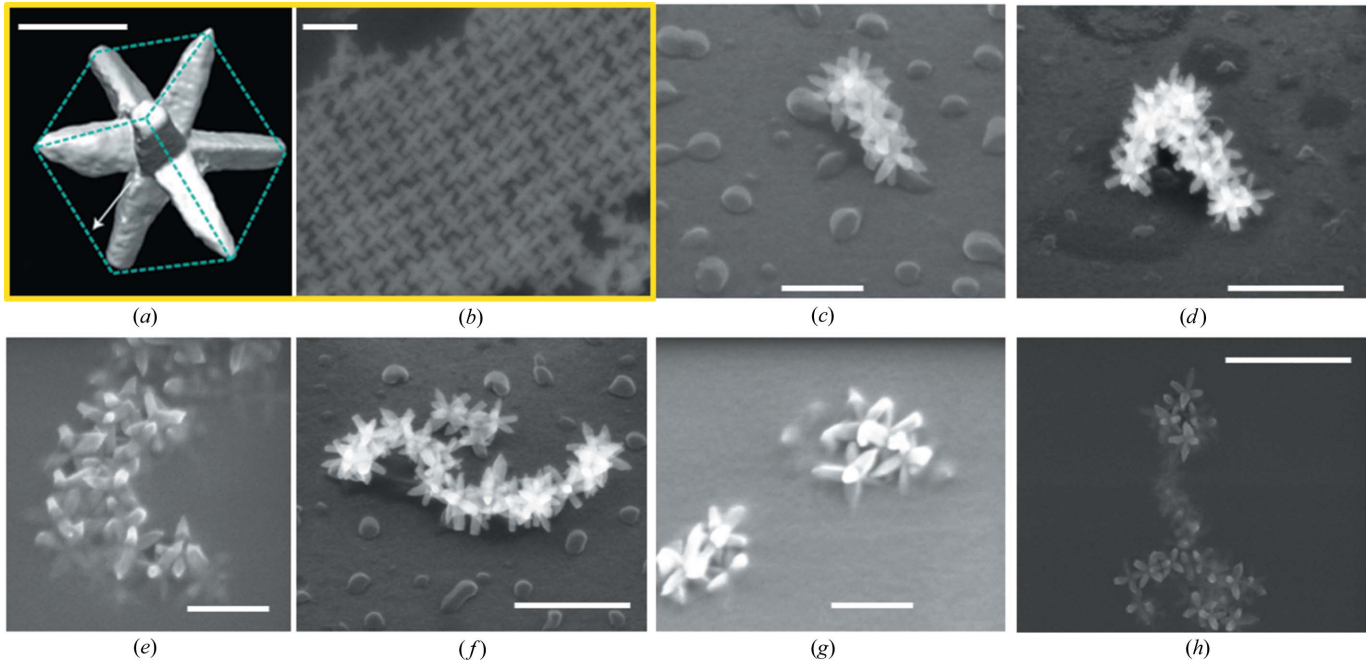

Figure 2
SEM images showing (*a*) a single CdSe/CdS octapod with pod length $L = 39 \pm 2$ nm and pod diameter $D = 12 \pm 2$ nm [reprinted with permission from Miszta *et al.* (2011)]; (*b*) a periodic 2D array of octapods [reprinted with permission of the International Union of Crystallography from De Caro *et al.* (2012)]; and (*c*)–(*h*) aperiodic architectures of octapods. Scale bars: (*a*) 40 nm; (*b*) 100 nm; (*c*) 100 nm; (*d*) 200 nm; (*e*) 100 nm; (*f*) 200 nm; (*g*) 100 nm; (*h*) 300 nm.

Table 1
Polymers used to prepare octapod-nanocomposite films.

Polymer	Polymer structure	MW (kg mol^{-1})	ρ (g ml^{-1})	T_g (K)
PMMA	$-[CH_2C(CH_3)(CO_2CH_3)]_n$	120–350	1.188	378
PS	$-[CH2CH(C6H5)]_n$	190–350	1.04	367

2% volume. The solutions were magnetically stirred for 15 min and poured into Al molds (30 × 10 × 3 mm) previously coated with a release agent (Marbocote 227) – 350 µl of the nanocomposite solution prepared with higher molecular weight (MW) polymers and 450 µl for polymers with low MWs. The nanocomposite solutions were allowed to dry at room temperature inside the glove box for 12 h. After drying the films were peeled off the substrates and cut into prismatic shapes of about 20 × 8 mm to obtain free-standing films. This protocol resulted in films with a thickness of 24 ± 4 µm. As a control, drops (15 µl) containing octapods without (labeled OCT) and with polymer were placed on Si_3N_4 membranes (window frame: 500 × 500 µm; thickness: 100 nm) on SiO_2 substrates of 10 × 10 × 1 mm and allowed to dry under the same conditions as the free-standing films.

3. Ptychographic coherent diffractive imaging experiment

The set of X-ray ptychography data was collected at the cSAXS beamline of the Swiss Light Source, at the Paul Scherrer Institut in Villigen, Switzerland. The most relevant technical details are as follows (De Caro *et al.*, 2016): the experiments were conducted with an X-ray beam of 6.2 keV (wavelength λ = 0.2 nm) using Fresnel zone plate primary optics with a diameter of 200 µm, deposited on a 200 nm-thick silicon nitride membrane, with an outermost zone width and a thickness of 50 and 500 nm, respectively. A 50 mm focal distance and a 50 µm depth of focus were established, and a piezoelectric stage was used for positioning the samples with nanometre resolution for the ptychography scans. A Pilatus

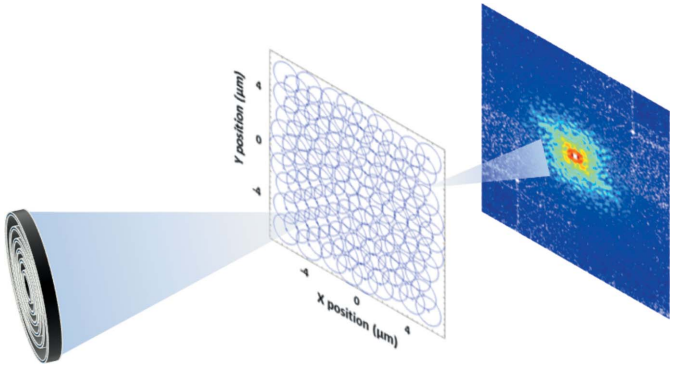

Figure 3
Ptychographic collection scheme illustrating the primary optics (here a Fresnel zone plate), the sample movement for each scan and the 2D diffraction pattern [reprinted with permission from Giannini *et al.* (2020)].

2M detector with $\Delta_{\text{det-pixel}}$ = 172 µm pixel was placed at z = 2.236 m from the sample, and the flight tube in between was filled with He to reduce air scattering and absorption. The sample was placed about 270 µm downstream of the focus, where the illumination was around 500 nm. According to the ptychographic collection scheme depicted in Fig. 3, each ptychography scan was realized along concentric circles with a radial step size of 0.2 µm and 5 points in the first circle. The exposure time per diffraction pattern was 0.2 s. A total area of 4 × 4 µm was scanned with a total of 324 acquired points per scan. However, as the samples are known to be sensitive to radiation dose, a precise acquisition scheme was followed. For each free-standing film, two different areas at 7 mm distance were investigated. Across each area, we acquired data from five 4 × 4 µm-large regions, positioned at relative distances of 50 µm from each other. The same region was scanned five times consecutively, producing a matrix of images {A*i*, B*i*, C*i*, D*i*, E*i*}, with i = 1–5 [further details are given by De Caro *et al.* (2016)]. It was these abundant data which allowed us to enhance the image contrast and improve the spatial resolution by averaging, denoising and deblurring the phased data after sub-pixel alignment.

4. The method

Phase information is lost in diffraction experiments. Only the amplitudes of complex waves can be measured. In ptychography the sample is scanned in coherent illumination mode, and each sample region has to be illuminated several times, and partially overlapped by neighboring regions, to have enough measured amplitude values for each sample point to compensate the lack of phase information. The coherent illumination of the entire Fresnel zone plate lens aperture, used to define the coherent illumination area on the sample, was ensured using a horizontal aperture close to the source. The focus size at the sample is d = 450 nm. As mentioned before, we used a wavelength of λ = 0.2 nm, so the obtained oversampling ratio $\lambda z/(2d\Delta_{\text{det-pixel}})$ = 2.9 is suitable for phase retrieval. Indeed, the Nyquist criterion requires an oversampling ratio larger than or equal to 2 (Nyquist, 1928) to compensate for scattering information related to the lost phase.

A difference map algorithm (Thibault *et al.*, 2009) with 200 iterations and a maximum likelihood optimization algorithm (Thibault & Guizar-Sicairos, 2012) with 100 iterations have been applied to each data set to firstly reconstruct the ptychographic maps and then refine the results. The reconstruction algorithm needs an initial probe, updated in each iteration; so we used the probe previously retrieved on a test specimen.

We evaluated the pixel size of a single-phase image. The effective area of the detector used for phasing being $N_{\text{det}} \times N_{\text{det}}$ = 192 × 192 pixels, the pixel size of the phased image is calculated as $\Delta_{\text{image-pixel}} = \lambda z/(N_{\text{det}}\Delta_{\text{det-pixel}}) \simeq 13.54$ nm. So the estimated spatial resolution of the phased maps would be of the order of $\rho \simeq \lambda/\text{NA} \simeq 2\Delta_{\text{image-pixel}} \simeq 27$ nm, NA being the numerical aperture: $\text{NA} = N_{\text{det}}\Delta_{\text{det-pixel}}/(2z)$ = 7.4 mrad.

The actual spatial resolution values would depend on the analyzed sample, if it scatters enough photons at the highest scattering angles; the noise level in the detector; eventual incoherent background signals; mechanical instabilities of the sample; radiation damage; and so on.

To estimate the actual spatial resolution of the phased images, we adopted the Fourier ring correlation (FRC) criterion (Heel & Schatz, 2005). FRC allows the evaluation of the correlation in the frequency space of two independent phase electron density maps to determine the resolution threshold at which the two images are best correlated. To evaluate the resolution, we used a broader accepted consistency criterion: the crossing point in the frequency domain between the FRC of two phased images I_1 and I_2 and the 'half-bit' threshold gives the maximum spatial frequency of the object details contained in images I_1 and I_2, which corresponds to a spatial resolution ρ. The intersection of the half-bit threshold curve with the FRC defines the point where there is a half-bit of information per pixel, per image, *i.e.* averaging the two independent images from which the FRC has been calculated, one bit of information per pixel is reached, summing the half-bit information obtained by each image. Here, $\rho = \Delta_{\text{image-pixel}}/(f/f_{\max})$, where $f_{\max}$ is the Nyquist frequency corresponding to the inverse of the area reconstructed with phasing. Our investigation indicates that $f/f_{\max}$ at the half-bit threshold curve ranges between 0.33 and 0.4 [see red curves in Figure S6 of the supporting information of De Caro *et al.* (2016)]. Therefore, the resolution of the phased maps ranges between 34 and 41 nm, *i.e.* between 2.5 and 3 times the $\Delta_{\text{image-pixel}}$ of the phased image, close to the estimated value of ρ = 27 nm (De Caro *et al.*, 2016). In fact, the spatial resolution of any microscopy image is actually limited by an effective point spread function (PSF) that very often can be well approximated by a Gaussian function and, usually, the spatial resolution is interrelated with the PSF full width at half-maximum (FWHM) (Koho *et al.*, 2019). In our phased maps one can put the standard deviations of the Gaussian SF equal to $\Delta_{\text{image-pixel}}$. Thus, the PSF FWHM would be $2.355\,\Delta_{\text{image-pixel}}$, *i.e.* about 32 nm, very close to the value determined by the FRC half-bit criterion.

In order to increase the quality of the retrieved maps, post image processing techniques have been applied to reduce the noise effect and better visualize the morphological information of the samples. Image contrast enhancement has been obtained by applying a routine based on the combination of deblurring and denoising stages. We used this approach to restore averaged ptychographical phased maps obtained for the same sample region. Very recently, with a similar approach of combining deblurring and denoising stages, spatial resolution improvements on single fluorescence microscopy images have also been shown (Koho *et al.*, 2019). Our approach is based on the classical total variation approach but with the addition of a bilateral filter regularization (Laghrib *et al.*, 2015). This combination leads to the preservation of the essential features of the image (De Caro *et al.*, 2016), such as boundaries and corners, which could be degraded using other approaches. In fact, both algorithms are devoted to denoising

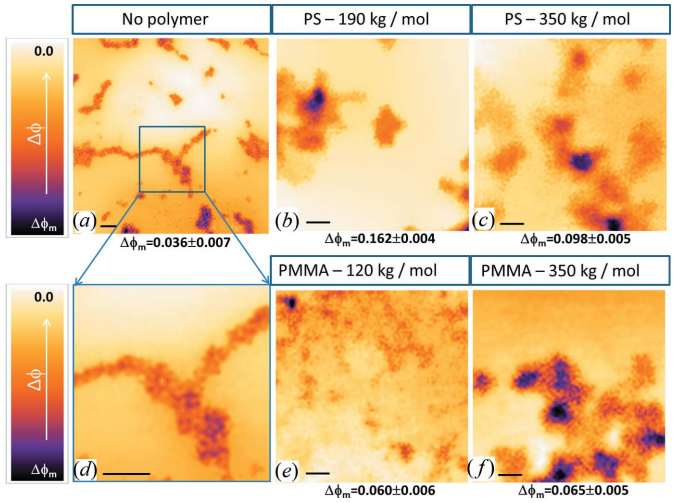

Figure 4
(*a*) OCT sample phase map; (*b*) PS-190 sample phase map; (*c*) PS-350 sample phase map; (*d*) enlargement of (*a*); (*e*) PMMA-120 sample phase map; (*f*) PMMA-350 sample phase map. Scale bars represent 200 nm. Phase errors have been estimated by considering the maximum and minimum $\Delta\phi_m$ values from five independent phased maps obtained in the same sample region. [Data on OCT and PS samples have been reprinted with permission from De Caro *et al.* (2016)].

the original image. The first is an iterative filter commonly used to reduce different types of additive or multiplicative noise while preserving sharp transitions. Essentially, it deconvolves a Gaussian point spread function, in our case one pixel large, from the original image in order to remove unwanted details (noise or spikes) whilst keeping important details such as edges. The second is an iterative filter that reduces noise, performing a nonlinear edge-preserving smoothing. The filtering procedure has been applied to the retrieved images. The results are shown in Fig. 4. After having partially deconvolved the PSF, the FRC half-bit resolution of the so-restored phased maps ranges between 27 and 20 nm, *i.e.* between 2 and 1.5 times the $\Delta_{\text{image-pixel}}$ of the phased image [see blue curves in Fig. S6 of the supporting information of De Caro *et al.* (2016)].

5. Results and discussion

The experiment was conducted on free-standing 24 ± 4 µm-thick films of PMMA (with 120 and 350 mg mol^{-1} molecular weights) and PS (with 190 and 350 mg mol^{-1} molecular weights) (see Table 1) containing networks of CdSe/CdS octapods [see Fig. 2(*a*)], as well as on the OCT control sample without polymer.

Fig. 4 shows the results of the phasing and post image processing for all analyzed samples. In the absence of thick polymer (OCT sample), the data reveal that the octapods aggregate with four pods in contact with the Si_3N_4 membrane, as revealed from the GISAXS data collected for this sample [Figure S3 of De Caro *et al.* (2016)] which presented intensity maxima clearly associated with the octapod symmetrical shape. In the case of thick polymers [Figs. 4(*a*)–4(*d*) taken from a previous study (De Caro *et al.*, 2016) and PMMA data

originally analyzed in the present work], octapods clearly form more intricate and irregular networks. The maximum phase shift ($\Delta\phi_m$) displayed for each image is a consequence of (i) the actual arrangement of the octapods inside the polymer, around the same thickness of 24 ± 4 μm, and (ii) the polymer molecular weight which somehow affects this arrangement. Here we found $\Delta\phi_m$ (PMMA-120) < $\Delta\phi_m$ (PMMA-350) < $\Delta\phi_m$ (PS-350) < $\Delta\phi_m$ (PS-190). The higher density of the material seems to affect the 3D assembly of the octapods. Indeed, at the same molecular weight of 350 kg mol^{-1}, the PS-350 [Fig. 4(*c*)] and PMMA-350 samples [Fig. 4(*f*)] show more 3D assemblies of octapods, which are at the origin of the darker regions in the maps with variable morphology. In contrast, the polymer with the lowest molecular weight [PMMA-120, Fig. 4(*e*)] shows predominantly a 2D arrangement of the octapods. In the PS-190 sample [Fig. 4(*b*)] we can see both 3D and 2D arrangements of the octapods. The values of the maximum phase shift ($\Delta\phi_m$) registered for this sample could be also caused by an abundant arrangement of octapods, which extends along the depth. The trend of the maximum phase shifts as a function of the sample composition, summarized in Fig. 4, has also been confirmed from the analysis of phased maps obtained from other regions of the investigated samples within the restrictions of the present experiment, *i.e.* that our phase reconstructions integrate the volume information in two dimensions.

6. Conclusions and perspectives

This work demonstrates the application of ptychography to the field of colloidal nanomaterials. Specifically, we proved ptychography to be effective for the study of the aggregation of nanocrystals in non-periodic architectures when buried in thick polymers. Such an unfavorable combination of non-periodic assembly and thick matrix (several tenths of a micrometre thick) rules out any direct imaging methods, such as SEM or TEM, which have severe limitations for investigating thick samples.

With the advent of fourth-generation radiation sources, or the upgrade of third-generation sources, X-ray coherent beams will gain in coherence and flux. This improvement will be extremely beneficial in similar experiments. Colloidal nanomaterials have recently found very interesting applications in nanomedicine, as they can be prepared and delivered in solution, and therefore easily administered to cells which are typically several-micrometre-thick matrices (Pelaz *et al.* 2017). The current and promising applications of nanomedicine include, but are not limited to, drug delivery, cell sorting and cell detection. In nanomedicine, a variety of organic/inorganic nanomaterials and devices are used. So far, there are over two dozen nanotechnology-based therapeutic products approved by the Food and Drug Administration for clinical use, and more are in clinical trials (Wagner *et al.*, 2006; Zhang *et al.*, 2008; Davis *et al.*, 2008). In cancer studies, much interest has been focused on understanding the internalization of nanoparticles in cells as a function of their size/shape and surface chemistry, as well as of the cell type. One of the most widely used methods to localize nanoparticles in cells and distinguish between internalized and externally adhered particles is confocal laser scanning microscopy (CLSM). CLSM allows visualization of nanoparticles in cells at 200 nm resolution, provided that the nanoparticles are marked with a fluorescent molecule, such as rhodamine. However, X-ray ptychography has the great advantage of being a label-free bio-imaging method, applied with success to investigate weakly scattering objects (Giewekemeyer *et al.*, 2010; Dierolf *et al.*, 2010) and biological cells (Jones *et al.*, 2013; Marrison *et al.*, 2013; Lima *et al.*, 2013) at 50 nm resolution (or better). In the present work, we imaged inorganic nanoparticles in ∼24 μm-thick polymers; but for future experiments, instead of thick polymers we could set up a project to image the fate of nanoparticles administrated to several-micrometre-thick cells, for example, at different time points, especially considering recent instrumentation and image processing developments for high-resolution ptychographic tomography (Holler *et al.*, 2018). Finally, in a number of recent studies, X-ray fluorescence was combined with ptychography to image frozen hydrated cells and, at the same time, map trace elements (S, P, K, Ca) in the unlabeled subcellular structures (Deng *et al.*, 2017). This combination of chemical and structural/topological information can be extremely useful in cancer studies, where the metabolism of trace elements is a key point.

Acknowledgements

Ana Diaz is gratefully acknowledged for setting up the experiment at the cSAXS beamline. The staff of the XRD2 beamline at LNLS-Campinas, in particular Leide Cavalcanti, Douglas Henrique Caetano de Araujo and Henrique Ferreira Canova, are acknowledged for their technical support during GISAXS data acquisition.

Funding information

The authors acknowledge financial support from the European Commission under the Seventh Framework Programme by means of the grant agreement for the Integrated Infrastructure Initiative (grant No. 262348), European Soft Matter Infrastructure (ESMI) an the CNR/CNpQ Italian–Brazilian bilateral agreement (X-ray mesocrystallographic studies of self-assembled 3D nanocrystal superlattices).

References

Akkerman, Q. A., Gandini, M., Di Stasio, F., Rastogi, P., Palazon, F., Bertoni, G., Ball, J. M., Prato, M., Petrozza, A. & Manna, L. (2016). *Nat. Energ.* **2**, 16194.
Akkerman, Q. A., Rainò, G., Kovalenko, M. V. & Manna, L. (2018). *Nat. Mater.* **17**, 394–405.
Alivisatos, P. (1997). *Endeavour*, **21**, 56–60.
Altamura, D., Holý, V., Siliqi, D., Lekshmi, I. C., Nobile, C., Maruccio, G., Cozzoli, P. D., Fan, L., Gozzo, F. & Giannini, C. (2012). *Cryst. Growth Des.* **12**, 5505–5512.
Altamura, D., Sibillano, T., Siliqi, D., De Caro, L. & Giannini, C. (2012). *Nanomater. Nanotechnol.* **2**, 16.

Billinge, S. J. L. & Levin, I. (2007). *Science*, **316**, 561–565.
Blanco, E., Shen, H. & Ferrari, M. (2001). *Nat. Biotechnol.* **33**, 941–951.
Boles, M. A., Engel, M. & Talapin, D. V. (2016). *Chem. Rev.* **116**, 11220–11289.
Castelli, A., de Graaf, J., Prato, M., Manna, L. & Arciniegas, M. P. (2016). *ACS Nano*, **10**, 4345–4353.
Corricelli, M., Altamura, D., Curri, M. L., Sibillano, T., Siliqi, D., Mazzone, A., Depalo, N., Fanizza, E., Zanchet, D., Giannini, C. & Striccoli, M. (2014). *CrystEngComm.* **16**, 9482–9492.
Craievich, A. F. (2016). *Handbook of Sol-Gel Science and Technology*, edited by L. Klein, M. Aparicio & A. Jitianu. Switzerland: Springer International Publishing.
Dahl, M., Liu, Y. & Yin, Y. (2014). *Chem. Rev.* **114**, 9853–9889.
Damasceno, P. F., Engel, M. & Glotzer, S. C. (2012). *Science*, **337**, 453–457.
Davis, M. E., Chen, Z. & Shin, D. M. (2008). *Nat. Rev. Drug Discov.* **7**, 771–782.
De Caro, L., Altamura, D., Arciniegas, M., Siliqi, D., Kim, M. R., Sibillano, T., Manna, L. & Giannini, C. (2016). *Sci. Rep.* **6**, 19397.
De Caro, L., Altamura, D., Vittoria, F. A., Carbone, G., Qiao, F., Manna, L. & Giannini, C. (2012). *J. Appl. Cryst.* **45**, 1228–1235.
Deng, J., Vine, D. J., Chen, S., Jin, Q., Nashed, Y. S. G., Peterka, T., Vogt, S. & Jacobsen, C. (2017). *Sci. Rep.* **7**, 445.
Dierolf, M., Thibault, P., Menzel, A., Kewish, C. M., Jefimovs, K., Schlichting, I., von König, K., Bunk, O. & Pfeiffer, F. (2010). *New J. Phys.* **12**, 035017.
Genç, A., Patarroyo, J., Sancho-Parramon, J., Bastús, N. G., Puntes, V. & Arbiol, J. (2017). *Nanophotonics*, **6**, 193–213.
Giannini, C., Holy, V., De Caro, L., Mino, L. & Lamberti, C. (2020). *Prog. Mater. Sci.* **112**, 100667.
Giannini, C., Ladisa, M., Altamura, D., Siliqi, D., Sibillano, T. & De Caro, L. (2016). *Crystals*, **6**, 87.
Giewekemeyer, K., Thibault, P., Kalbfleisch, S., Beerlink, A., Kewish, C. M., Dierolf, M., Pfeiffer, F. & Salditt, T. (2010). *Proc. Natl Acad. Sci. USA*, **107**, 529–534.
Glatter, O. (2018). *Scattering Methods and their Application in Colloid and Interface Science*. Amsterdam: Elsevier.
Gordon, T. R., Diroll, B. T., Paik, T., Doan-Nguyen, V. V. T., Gaulding, E. A. & Murray, C. B. (2015). *Chem. Mater.* **27**, 2502–2506.
Gupta, S. M. & Tripathi, M. A. (2011). *Chin. Sci. Bull.* **56**, 1639–1657.
Heel, M. van & Schatz, M. (2005). *J. Struct. Biol.* **151**, 250–262.
Holler, M., Raabe, J., Diaz, A., Guizar-Sicairos, M., Wepf, R., Odstrcil, M., Shaik, F. R., Panneels, V., Menzel, A., Sarafimov, B., Maag, S., Wang, X., Thominet, V., Walther, H., Lachat, T., Vitins, M. & Bunk, O. (2018). *Rev. Sci. Instrum.* **89**, 043706.
Jones, M. W. M., Elgass, K., Junker, M. D., Luu, M. B., Ryan, M. T., Peele, A. G. & van Riessen, G. A. (2013). *Sci. Rep.* **3**, 2288.
Juhás, P., Cherba, D. M., Duxbury, P. M., Punch, W. F. & Billinge, S. J. L. (2006). *Nature*, **440**, 655–658.
Kim, M. R., Miszta, K., Povia, M., Brescia, R., Christodoulou, S., Prato, M., Marras, S. & Manna, L. (2012). *ACS Nano*, **6**, 11088–11096.
Koho, S., Tortarolo, G., Castello, M., Deguchi, T., Diaspro, A. & Vicidomini, G. (2019). *Nat. Commun.* **10**, 3103.
Kumar, C. S. S. R. (2016). *X-ray and Neutron Techniques for Nanomaterials Characterization*. Berlin, Heidelberg: Springer–Verlag.
Laghrib, A., Hakim, A. & Raghay, S. (2015). *EURASIP J. Image Vid.* **2015**, 19.
Lima, E., Diaz, A., Guizar-Sicairos, M., Gorelick, S., Pernot, P., Schleier, T. & Menzel, A. (2013). *J. Microsc.* **249**, 1–7.
Marrison, J., Räty, L., Marriott, P. & O'Toole, P. (2013). *Sci. Rep.* **3**, 2369.
Mino, L., Borfecchia, E., Segura-Ruiz, J., Giannini, C., Martinez-Criado, G. & Lamberti, C. (2018). *Rev. Mod. Phys.* **90**, 025007.
Miszta, K., de Graaf, J., Bertoni, G., Dorfs, D., Brescia, R., Marras, S., Ceseracciu, L., Cingolani, R., van Roij, R., Dijkstra, M. & Manna, L. (2011). *Nat. Mater.* **10**, 872–876.
Muller-Buschbaum, P. (2003). *Anal. Bioanal. Chem.* **376**, 3–10.
Noel, N. K., Stranks, S. D., Abate, A., Wehrenfennig, C., Guarnera, S., Haghighirad, A.-A., Sadhanala, A., Eperon, G. E., Pathak, S. K., Johnston, M. B., Petrozza, A., Herz, L. M. & Snaith, H. J. (2014). *Energy Environ. Sci.* **7**, 3061–3068.
Nugent, K. A. (2010). *Adv. Phys.* **59**, 1–99.
Nyquist, H. (1928). *Trans. AIEE*, **47**, 617–644.
Paik, T. & Murray, C. B. (2013). *Nano Lett.* **13**, 2952–2956.
Parak, W. J., Gerion, D., Pellegrino, T., Zanchet, D., Micheel, C., Williams, S. C., Boudreau, R., Gros, M. A. L., Larabell, C. A. & Alivisatos, A. P. (2003). *Nanotechnology*, **14**, R15–R27.
Pelaz, B., Alexiou, C., Alvarez-Puebla, R. A., Alves, F., Andrews, A. M., Ashraf, S., Balogh, L. P., Ballerini, L., Bestetti, A., Brendel, C., Bosi, S., Carril, M., Chan, W. C. W., Chen, C., Chen, X., Chen, X., Cheng, Z., Cui, D., Du, J., Dullin, C., Escudero, A., Feliu, N., Gao, M., George, M., Gogotsi, Y., Grünweller, A., Gu, Z., Halas, N. J., Hampp, N., Hartmann, R. K., Hersam, M. C., Hunziker, P., Jian, J., Jiang, X., Jungebluth, P., Kadhiresan, P., Kataoka, K., Khademhosseini, A., Kopeček, J., Kotov, N. A., Krug, H. F., Lee, D. S., Lehr, C.-M., Leong, K. W., Liang, X.-J., Ling Lim, M., Liz-Marzán, L. M., Ma, X., Macchiarini, P., Meng, H., Möhwald, H., Mulvaney, P., Nel, A. E., Nie, S., Nordlander, P., Okano, T., Oliveira, J., Park, T. H., Penner, R. M., Prato, M., Puntes, V., Rotello, V. M., Samarakoon, A., Schaak, R. E., Shen, Y., Sjöqvist, S., Skirtach, A. G., Soliman, M. G., Stevens, M. M., Sung, H.-W., Tang, B. Z., Tietze, R., Udugama, B. N., VanEpps, J. S., Weil, T., Weiss, P. S., Willner, I., Wu, Y., Yang, L., Yue, Z., Zhang, Q., Zhang, Q., Zhang, X.-E., Zhao, Y., Zhou, X. & Parak, W. J. (2017). *ACS Nano*, **11**, 2313–2398.
Peng, X., Manna, L., Yang, W., Wickham, J., Scher, E., Kadavanich, A. & Alivisatos, A. P. (2000). *Nature*, **404**, 59–61.
Petronella, F., Truppi, A., Ingrosso, C., Placido, T., Striccoli, M., Curri, M. L., Agostiano, A. & Comparelli, R. (2017). *Catal. Today*, **281**, 85–100.
Reiss, C. A., Kharchenko, A. & Gateshki, M. (2012). *Z. Kristallogr.* **227**, 257–261.
Renaud, G., Lazzari, R. & Leroy, F. (2009). *Surf. Sci. Rep.* **64**, 255–380.
Rodenburg, J. M., Hurst, A. C., Cullis, A. G., Dobson, B. R., Pfeiffer, F., Bunk, O., David, C., Jefimovs, K. & Johnson, I. (2007). *Phys. Rev. Lett.* **98**, 034801.
Rogach, A. L. (2008). *Semiconductor Nanocrystal Quantum Dots*. New York: SpringerWein.
Scher, E. C., Manna, L. & Alivisatos, A. P. (2003). *Philos. Trans. A Math. Phys. Eng. Sci.* **361**, 241–255.
Shapiro, D. A., Yu, Y.-S., Tyliszczak, T., Cabana, J., Celestre, R., Chao, W., Kaznatcheev, K., Kilcoyne, A. L. D., Maia, F., Marchesini, S., Meng, Y. S., Warwick, T., Yang, L. L. & Padmore, H. A. (2014). *Nat. Photon.* **8**, 765–769.
Shi, X., Burdet, N., Chen, B., Xiong, G., Streubel, R., Harder, R. & Robinson, I. K. (2019). *Appl. Phys. Rev.* **6**, 011306.
Sommariva, M. (2013). *Solid State Phenom.* **203–204**, 17–20.
Svergun, D. I. & Koch, M. H. J. (2003). *Rep. Prog. Phys.* **66**, 1735–1782.
Talapin, D. V., Shevchenko, E. V., Bodnarchuk, M. I., Ye, X., Chen, J. & Murray, C. B. (2009). *Nature*, **461**, 964–967.
Tao, A. R., Habas, S. & Yang, P. (2008). *Small*, **4**, 310–325.
Thibault, P., Dierolf, M., Bunk, O., Menzel, A. & Pfeiffer, F. (2009). *Ultramicroscopy*, **109**, 338–343.
Thibault, P. & Guizar-Sicairos, M. (2012). *New J. Phys.* **14**, 063004.
Wagner, V., Dullaart, A., Bock, A. K. & Zweck, A. (2006). *Nat. Biotechnol.* **24**, 1211–1217.
Yu, Y., Yu, D., Sadigh, B. & Orme, C. A. (2018). *Nat. Commun.* **9**, 4211.